

# Green Light Photoelectrocatalysis with Sulfur-Doped Carbon Nitride: Using Triazole-Purpald for Enhanced Benzylamine Oxidation and Oxygen Evolution Reactions

Maria Jerigova <sup>1</sup>✉, Yevheniia Markushyna <sup>1</sup>✉, Ivo F. Teixeira <sup>1,2</sup>, Bolortuya Badamdorj <sup>1</sup>, Mark Isaacs <sup>3,4</sup>, Daniel Cruz <sup>5</sup>, Iver Lauermann <sup>6</sup>, Miguel Ángel Muñoz-Márquez <sup>7</sup>, Nadezda V. Tarakina <sup>1</sup>, Nieves López-Salas <sup>1</sup>, Oleksandr Savateev <sup>1</sup>, Pablo Jimenéz-Calvo <sup>1,\*</sup>

\*Corresponding author: [pablo.jimenez-calvo@mpikg.mpg.de](mailto:pablo.jimenez-calvo@mpikg.mpg.de)

<sup>1</sup> Department of Colloid Chemistry, Max-Planck-Institute of Colloids and Interfaces, Am Mühlenberg 1, 14476 Potsdam, Germany

<sup>2</sup> Department of Chemistry, Federal University of São Carlos, 13565-905, São Carlos, SP, Brazil

<sup>3</sup> HarwellXPS, Research Complex at Harwell, Rutherford Appleton Lab, Didcot OX11 0FA, United Kingdom

<sup>4</sup> Department of Chemistry, University College London, 20 Gower Street, London, WC1H 0AJ, United Kingdom

<sup>5</sup> Department of Inorganic Chemistry, Fritz-Haber-Institut der Max-Planck-Gesellschaft, Faradayweg 4–6, 14195 Berlin, Germany

<sup>6</sup> Helmholtz-Zentrum Berlin für Materialien und Energie, Department PVcomB, Schwarzschildstraße 3, 12489 Berlin, Germany

<sup>7</sup> Chemistry Division, School of Science and Technology, University of Camerino, Via Madonna delle Carceri, Italy

## Abstract

Novel high performing materials will dictate the pace of reinventing industrial chemical processes to attain desired carbon neutrality targets. Regarding the urgency of exploiting solar irradiation long range visible-light photoelectrocatalysts from abundant resources will play a key role in the aforementioned effort. Anionic doping via co-polymerization and pre-organization of precursors results in tuneable and extrinsic semiconductors, making this a highly attractive methodology. Triazole derivative-purpald, an unexplored precursor but sulfur (S) container, combined with melamine during one solid-state polycondensation reaction with two thermal steps leads to S-doped carbon nitrides (C<sub>3</sub>N<sub>4</sub>). The series of S-doped/C<sub>3</sub>N<sub>4</sub>-based materials demonstrated enhanced optical, electronic, structural, geometric, textural, and morphological properties and exhibited higher performance in organic benzylamine photooxidation, oxygen evolution, and similar storing energy (capacitor brief investigation) than references. Among the five composites, 50M-50P exhibited the highest photooxidation conversion yield (84±3%) of benzylamine to imine at 535 nm – green light for 48h, due to an extra discrete shoulder reaching ~700 nm, an unusual high sulfur content, preservation of crystal size, new intraband energy states, rare deep structural defects by layer distortion, hydrophobic surface, low porosity, and 10-16 nm pores. An in-depth analysis of S doping was investigated coupling x-ray photoelectron spectroscopy, transmission electron microscope, and elemental analysis, providing insights on bonds, distribution, and surface/bulk content. This work contributes to the development of amorphous photocatalysts with long-visible-light range for solar energy conversion and storage.

**Keywords:** photoelectrocatalyst, co-polymerization, doping, purpald, carbon nitride, benzylamine, oxygen

## 1. Introduction

Sustainable conversion of chemicals and green renewable energies are in high demand to meet proposed decarbonization targets.<sup>[1]</sup> Existing industrial processes must be reinvented, and functional, stable, cheap, and abundant materials should be delivered to lower energetic and economical costs.<sup>[2]</sup> Undoubtedly, the new generation of long-range visible light high-performing photoactive materials will play a key role in utilizing a significant portion of the solar spectrum while working under ambient conditions.<sup>[3]</sup> The American Society of Materials<sup>[4]</sup> points out that the visible light irradiating the Earth's surface is ~43% of the total photons, thus representing the largest portion available (Air Mass 1.5 Spectra). The relevance of efficient visible light catalysts is driven by the urgency to exploit the sun's light (an abundant source).<sup>[3]</sup>

Photoelectrocatalysis is a leading field with the potential to unleash numerous noteworthy technological deliveries.<sup>[5]</sup> Benchmark oxidative photocatalysis and photoelectrochemical cells (PEC) are of great interest to move forward the field in two directions: (a) shifting conventional chemical processes and (b) finding higher yields of solar-to-photon energy conversion for building block molecules or producing energy vectors. With respect to technological viability as a large scale implementation; one of the significant bottlenecks in the field is ensuring the materials in question are highly efficient light absorbers.<sup>[6]</sup>

Metal-free, abundant, easy to modify, and active single-catalyst are suitable candidates for diverse applications in photo- and electro-catalytic processes.<sup>[6]</sup> A notable and simple route for the photoactivated production of added value product is that of photocatalytic oxidation of benzylamine to dibenzylimine. Imines and their derivatives are important building blocks for the synthesis of several heterocyclic systems (imidazoles and palladacycles) and linear molecules (oximes and hydrazones) mainly used in the pharmaceutical and physiology industries with a market of ~1 billion EUR and an annual growth of 11%.<sup>[7]</sup> Though the conventional organic synthesis to obtain imines using metal salts based on aluminum, copper, nickel, or platinum results in high yields (80-95 %)<sup>[8]</sup>, their protocols consist of thermal reflux and removal of water, making it costly and time-consuming. Alternatively, photocatalysis can reach the same yields (~90%) through one-pot chemistry using simple control of atmosphere, substrate, light, and a "metal-free" catalyst highlighting its wide-scale feasibility by being a faster and greener process.

For photoelectrochemical oxygen evolution (OER), the reaction occurs in the anode of the electrolyzer. Yet, to this day, current state-of-the-art of OER catalysts are based on metals such as iridium,<sup>[9,10]</sup> ruthenium,<sup>[11]</sup> iron oxides,<sup>[12,13]</sup> and others,<sup>[14,15]</sup> which are non-viable in the long term due to the high-cost and scarcity of raw materials, and dissolution problems.<sup>[16]</sup> Thus, replacement of traditional OER catalysts with organic semiconductors (SC) is an appealing strategy to mitigate the dependency on metal oxides.

Current metal-free catalysts are graphene,<sup>[17]</sup> covalent organic frameworks,<sup>[18]</sup> carbon nanotubes,<sup>[19]</sup> graphdiyne,<sup>[20]</sup> and carbon nitrides (C<sub>3</sub>N<sub>4</sub>).<sup>[21]</sup> Among them, C<sub>3</sub>N<sub>4</sub> is an appealing SC due to its medium band gap, *e.g.*, 2.7 eV that enables capture photons from 460 nm and below.<sup>[22]</sup> Though activities are still rather low because of (a) low absorption of photons in the visible range of the spectrum (b) low charge carrier mobility, limited by the lack of interlayer hybridization (c) its valence band position being too close to the O<sub>2</sub>/H<sub>2</sub>O potential, hindering water oxidation, (d) high recombination, (e) low surface area, etc.<sup>[21,23]</sup>

Nanoarchitecture tailoring of C<sub>3</sub>N<sub>4</sub> structural, geometric, electronic, and optical properties has been exhaustively investigated using four main strategies: templating, copolymerization, exfoliation, and element doping.<sup>[24,25]</sup> Such approaches aim at orienting planar bonding, symmetric interlayer interactions, control porosity, specific morphology, defined microstructure, and high surface area.<sup>[24,25]</sup>

Element doping via co-polymerization and pre-organization of precursor molecules is one promising route to achieving controlled and tuned C<sub>3</sub>N<sub>4</sub> materials.<sup>[26]</sup> Recently, unconventional aminotriazoles

(enhancers of visible light absorption) precursors containing sulfur (S) based groups have emerged to tune the  $C_3N_4$  band gap effectively.<sup>[27–30]</sup> The doped S-atom may serve as (a) heteroatom active/trap site (b) electron donor (c) lattice distorter due to its large size (d) polarizer to a lesser extent due to its p orbital disposition.<sup>[23,31–33]</sup> Typical monomers are thiourea and trithiocyanuric acid, limiting the insertion of S in the  $C_3N_4$  lattice, owing to S moieties tending to leave upon calcination.<sup>[23,24,34,35]</sup> In an attempt to preserve S atoms within an amorphous photo-electric  $C_3N_4$  lattice, purpald, an unexplored triazole-sulfur-containing molecule<sup>[36]</sup> is used to synthesize S-doped/ $C_3N_4$  multifunctional materials.

Herein, a one-pot solid-state reaction using different purpald/melamine ratios is applied to obtain five composites and two references. The resulting S-doped/ $C_3N_4$ -based composites displayed improved optical, electronic, structural, geometric, textural, and morphological properties compared with  $C_3N_4$  references. They were tested in two photo-/photoelectrocatalytic reactions: benzylamine oxidation and oxygen evolution. The innovative strategy consists of using sulfur-containing purpald, an unexplored molecule to dope the resulting carbon nitrides in different proportions, distributions, and bulk and surface nominal quantities. This study reports the use of purpald for the first time in literature, to the best of our knowledge.

## 2. Results and discussion

### 2.1. Solid-state reaction insights: formation path and elimination mechanism

To understand the formation of final hybrid carbon nitrides of this study, scientific criteria of the selected thermal steps of the reaction, pre-organization of the precursor molecules, reaction mass yields, and TGA-MS of the two precursors and the seven  $C_3N_4$  materials were investigated. The nomenclature description of the  $C_3N_4$  composites is based on the initial precursors' ratio, for example 10M-90P, where M stands for melamine (10 wt. %) and P for purpald (90 wt. %).

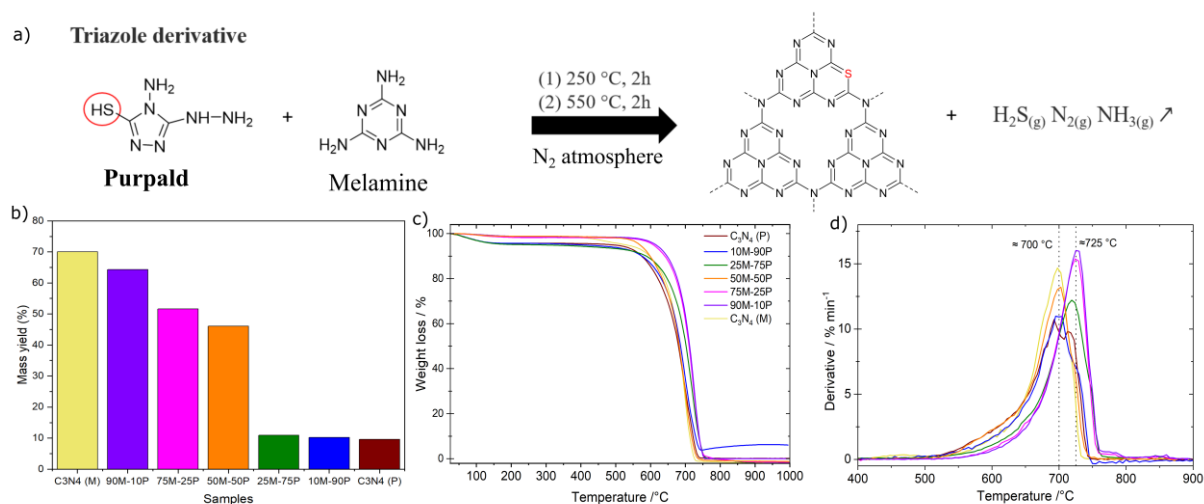


**Figure 1.** a) Synthetic path of the as-prepared amorphous S-doped/ $C_3N_4$  with their elimination mechanism, b) Mass yield percentages, c) TGA profiles and d) derivatives of all the series of the five composites and two references.

The one-pot solid-state reaction in **Fig. 1a** illustrates the combination of purpald and melamine precursors treated at two thermal steps under a nitrogen ( $N_2$ ) atmosphere, resulting in S-doped/ $C_3N_4$ . The elimination mechanism is tentatively proposed as releasing the typical  $N_2$  and  $NH_3$  gases but also hydrogen sulfide ( $H_2S$ ) due to the thiol group presence in the purpald molecule. Such a reaction aims to drive a pre-orientation of the monomer precursors prior to the polycondensation. The two thermal steps serve to different purposes, with the first step at 250 °C is intended to solubilize purpald at 22 °C higher than its melting point (228 °C, Sigma Aldrich spreadsheet) to form a liquid phase that entangles the melamine powder and creates an interface contact, promotes synergistic effects at molecular level (only valid for the composites). Upon reaching 343 °C melamine melts,<sup>[37]</sup> though as it is part of the

thermal ramp the influence upon reaction is not as relevant as the stationary step at 250 °C, promoting the liquid-solid contact. Finally, 550 °C, is the well-reported temperature at which the C<sub>3</sub>N<sub>4</sub> heptazine polymeric chain is formed.<sup>[38-41]</sup>

TGA profiles reveal the kinetic decomposition investigation of the C<sub>3</sub>N<sub>4</sub> precursors. A brief study mimicking the solid-state reaction shows the difference between the decomposition of melamine and purpald under a N<sub>2</sub> atmosphere. The purpald decomposition occurs in three steps at 236, 511, and 665 °C with mass losses of 40, 5, and 55%, respectively as illustrated in **Fig. S1a**. As this precursor is not listed in among typical carbon nitride N rich precursors, we have to attributed the three decomposition steps to the arrangement/formation of melamine, melem to melon transition, and the 2D polymeric network of C<sub>3</sub>N<sub>4</sub> heptazine, as elucidated by Lau and Lotsch.<sup>[40]</sup> For the case of melamine decomposition, it occurs in single step as illustrated in **Fig. S1b**, where all mass is lost at 340 °C consistent with the theoretical melting point occurring at 350-354 °C.<sup>[37]</sup>

The reaction mass yields were calculated when dividing the mass of the material recuperated after the thermal reaction in the crucible by the initial mass of the precursor(s) as noted in equation 1.

$$\% \text{ mass yield} = \frac{m_{\text{after thermal reaction}}}{m_{\text{initial precursor(s)}}} \quad (1)$$

The reaction mass yields of the resulting C<sub>3</sub>N<sub>4</sub> (**Fig. 1b**) provide a combination of a quasi-linear descending trend ( $\leq 50$  % purpald) and a constant trend ( $\geq 75$  % purpald). When higher amount of melamine (alone or mixed with purpald) was added, a higher mass was recovered following thermal synthesis. The latter, happens presumably due to the quenching sublimation effect thanks to the formation of new covalent bonds (heptazine formation) in both vertical and horizontal directions.<sup>[25]</sup> Surprisingly, purpald alone and high purpald content ( $\leq 75\%$ ) composites produces  $\sim 10\%$  mass yield, providing a material of lower density. For instance, the mass yield trend indicates two possible effects in the function of the varying precursor ratio: at high content of melamine ( $\geq 50\%$ ) the C<sub>3</sub>N<sub>4</sub> preserves the quenching effect and at low content of melamine ( $\leq 25\%$ ), or majority purpald content, the C<sub>3</sub>N<sub>4</sub> composites experiences an accelerated sublimation resulting in only 10% of mass recovery.

TGA profiles of all the materials (**Fig. 1c**) suggest that the thermal decomposition occurs in a one-pot decomposition step, resulting in a quasi-symmetrical peak in their respective derivatives **Fig. 1d**. The decomposition starts progressively with a prolong tail starting at  $\sim 500$  °C and finalize with a pronounced decay at 775 °C, suggesting destabilization of the 2D structure materials begins gradually at lower temperatures before an abrupt decay above  $\sim 700$  °C. The temperature of the peak was observed at 700-725 °C, suggesting the presence of the interconnected heptazines (typical for polymeric C<sub>3</sub>N<sub>4</sub>), as has been previously reported in C<sub>3</sub>N<sub>4</sub> studies.<sup>[42,43]</sup>

Typical ammonia (NH<sub>3</sub>) and N<sub>2</sub> gas traces from the C<sub>3</sub>N<sub>4</sub> materials were monitored by TGA-mass spectroscopy (**Fig. S2**). A third MS trace at  $m/z = 34$  was monitored – ascribed to be H<sub>2</sub>S, produced from the thiol group of the purpald precursor. We believe that the release of H<sub>2</sub>S gas in autogenous conditions can lead to a self-porogen effect of variable extent, as a function of purpald ratio.

Thanks to the H<sub>2</sub>S gas monitored (elimination mechanism), two hypotheses in the thiol chemistry functionality risen. Purpald thermal decomposition drives two benefits within this synthetic procedure: S-doping in the C<sub>3</sub>N<sub>4</sub> lattice and gaseous H<sub>2</sub>S release acting as self-porogen agent.

## 2.2. Physicochemical characterization

To investigate and identify the dominant physicochemical properties of the resulting hybrid C<sub>3</sub>N<sub>4</sub> composites in association with their performances a series of routine and advanced characterization techniques were performed. Optical and electronic properties were analyzed through a combinatorial approach of UV-vis-NIR, Photoluminescence (PL), and electrochemical Mott-Schottky measurements.

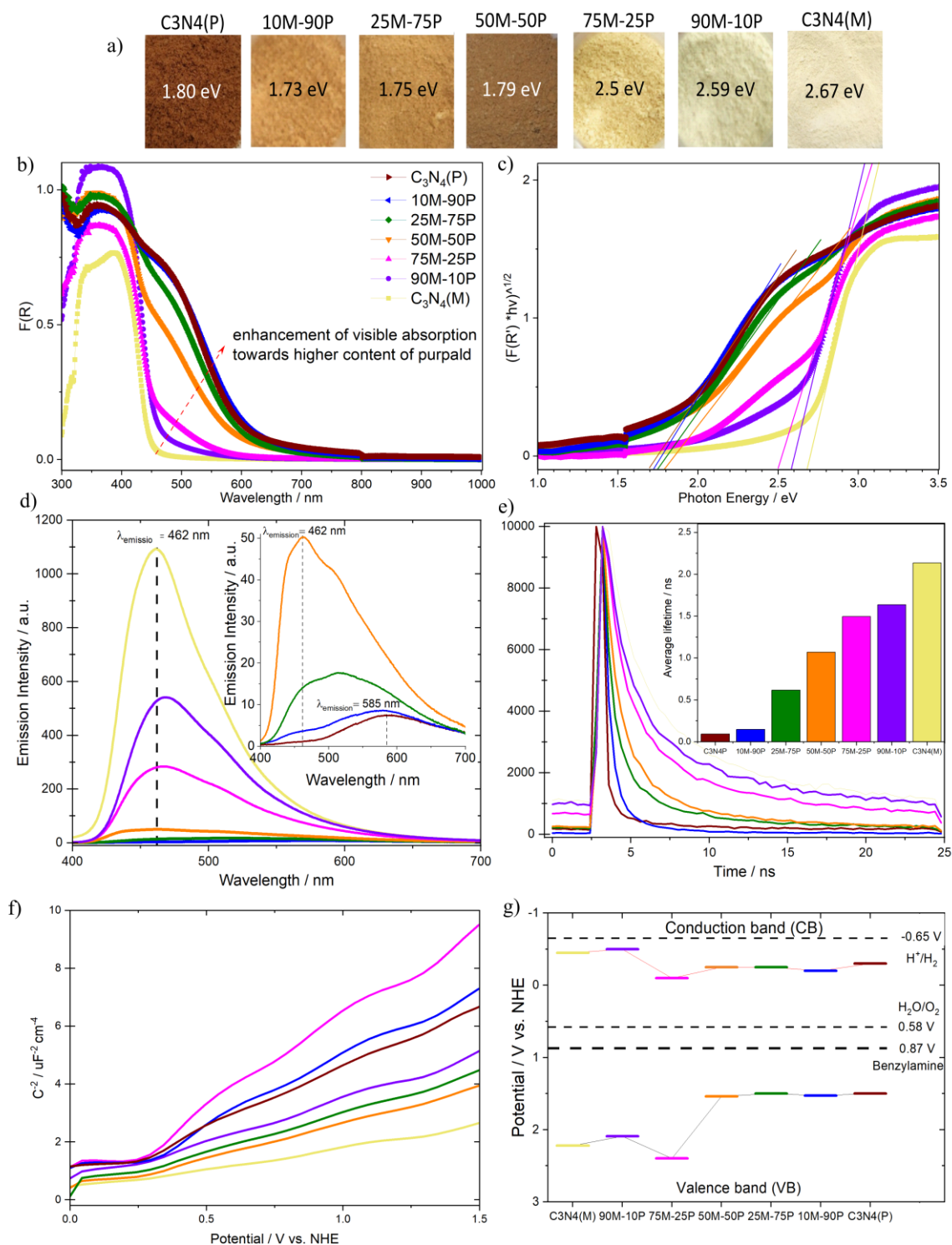


**Figure 2.** a) Color of the material powders of the five composites and two references with their optical band gap (extracted from Tauc plot), b) UV-vis spectra, c) Tauc plot, d) steady state PL spectra (inset) zoom of the samples with high purpald content, e) transient PL spectra (Inset shows average lifetime quantification), f) Mott-Schottky plot g) flat band potential diagram of all the as-prepared samples.

**Fig. 2a** shows the color of each as-prepared sample. An observable trend from pale yellow ( $C_3N_4(M)$ ) to reddish orange ( $C_3N_4(P)$ ) is found. The two composites with highest content of melamine  $\geq 75\%$  remained in the yellow range while the other three composites with high content of purpald  $\geq 50\%$  are orange/brownish, demonstrating that the mixing of melamine and purpald in different proportions results in tuneable optical properties. The UV-vis-NIR spectra (**Fig. 2b**) reports the typical maximum absorption of  $C_3N_4$  materials in the UV/blue range for all seven materials. Such a maximum is

commonly associated with the absorption band edge at ~455 nm, which in our study applies to all samples, though particularly for C<sub>3</sub>N<sub>4</sub>(M), 90M-10P, and 75M-25P. This absorbance is ascribed to  $\pi \rightarrow \pi^*$  electron transitions of the aromatic  $\pi$ -conjugated systems constituted of interconnected heptazine units.<sup>[44-46]</sup> Although the two composites with low purpald content ( $\leq 25\%$ ) exhibited a slight tail towards visible - samples with high purpald content ( $\geq 50\%$ ) transform the forementioned tail into a discrete shoulder towards higher wavelengths. This shoulder lacks a clear maximum but displays a red shift absorption band edge at 690-715 nm (representing ~250 nm shift) equivalent to photon energies ranging from 1.7 to 1.8 eV. These photon energy values are consistent with the obtained optical band gaps by Tauc plot in **Fig. 2c** and **Table S1**.

The observed tail/shoulder in the visible region may come from two associated contributions: (a) S atoms substitution and b)  $n \rightarrow \pi^*$  electronic transitions. (a) Due to the S larger size compared with C or N, S introduction in the C<sub>3</sub>N<sub>4</sub> structure caused a significant lattice distortion<sup>[32]</sup> and introduce a noticeable expansion effect or pronounced tilt angularity. Such distortion leads to new potential interactions in addition to Van der Waals, as an interplanar layer interaction/angularity is induced. A secondary reason should be considered to a lesser extent: the  $p_x$  and  $p_y$  orbitals of the introduced S atoms that partially donate electron density to the point of polarizing the s orbitals of the neighboring C or N atom, promoting new intraband energy states,<sup>[32]</sup> despite the minimal electronegativity differences of S (2.5), C (2.5), and N (3.0) atoms.<sup>[32,47]</sup> The second potential contribution (b) has been attributed to  $n \rightarrow \pi^*$  forbidden electronic transitions, ascribed to a more pronounced layer deformation that results in a more distorted in-plane configuration<sup>[48-50]</sup> where electron lone pairs of the nitrogen edge atoms in the C<sub>3</sub>N<sub>4</sub> skeleton are those responsible.<sup>[36]</sup>

In addition to these two explanations, secondary absorption bands at longer wavelengths have been recently studied for potassium poly heptazine imide (K-PHI) systems, another member of the C<sub>3</sub>N<sub>4</sub> family.<sup>[51,52]</sup> The noticeable shoulder was defined as the intraband states of this material that takes part in energy transfer reactions, typically with oxygen, under green or red irradiation. Therefore, we posit that, similar behavior be expected for the composites studied in this work. Overall, these new reddish orange materials ( $\geq 50\%$  purpald) display an outstanding long-range absorption in the visible range of the spectrum. This red-shift enhancement of absorption is confirmed by color tuning from pale yellow to reddish orange and additional small intra band energy states signals.

Steady state PL spectra (**Fig. 2d**) of the C<sub>3</sub>N<sub>4</sub> present two different peaks and PL intensities vary among the samples underpinning their disparity in crystallinity. The first pronounced broad peak, centered at 462 nm was ascribed as the maximum emission for the most crystalline samples: C<sub>3</sub>N<sub>4</sub>(M) and the composites with  $\geq 50\%$  of melamine. Subsequently, the PL intensity of the primary peak (462 nm) for the C<sub>3</sub>N<sub>4</sub> purpald-derivatives start decreasing when increasing the purpald content ( $\geq 25\%$ ) relative to the highest emission of the C<sub>3</sub>N<sub>4</sub>(M) (the most crystalline material). Nevertheless, the 50M-50P composite is the frontier at which high purpald content ( $>50\%$ ) composites exhibit the second visible peak. Following the progressive apparition of the secondary peak centered at ~585 nm (representing ~123 nm shift), concomitant with a noticeable red shift, this suggests a more efficient photo-induction of charge carriers separation occurring attributed to the reduction of charge density of the charge carrier traps, possibly by electron delocalization on surface terminal sites, evidencing how weak is the radiative recombination.<sup>[34,36]</sup> The red shift is particularly significant for the 10M-90P composite and C<sub>3</sub>N<sub>4</sub>(P) reference, highlighting the enhancement of light absorption at longer wavelengths that may originate from the increase of structural defects, presumably by their amorphous nature. These defects have been reported as new deep-level traps for non-radiative recombination, and electronic modulation properties in these new materials are expected.<sup>[36,53]</sup>

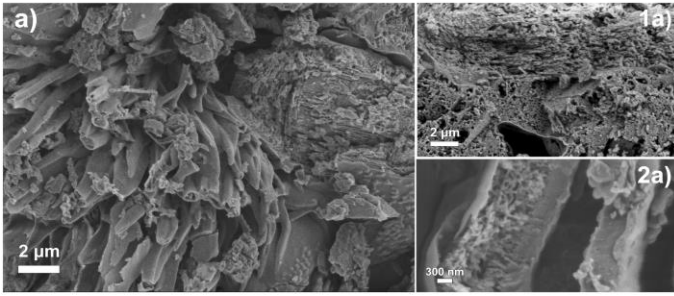
Transient PL spectra (**Fig. 2e**) display the lifetime of the charge carriers involved after the material was excited with a 375 nm energy pulse. A linear descending trend starting at the reference C<sub>3</sub>N<sub>4</sub>(M) that exhibits the longest average lifetime charge carrier, 2.13 ns (**Table S1**). The linear decay is

followed with increasing of the purpald content (and associated sulfur doping) in the composites, and the reference  $C_3N_4(P)$  exhibits the shortest average lifetime charge carrier, 0.09 ns.

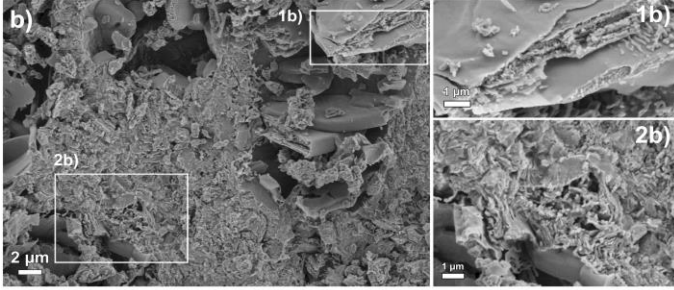
Mott-Schottky plots (**Fig. 2f**) serve to determine the flat band potentials and reveal how the mixture of precursors affects the electronic band structures of the as-prepared samples. The Mott-Schottky plots exhibited positive slopes, typically ascribed for n-type SC.<sup>[15,36,54]</sup> The flat band potentials were the conduction band (CB) position of each studied photoelectrode. In turn, the valence band (VB) positions were determined by subtracting the band gap from the CB. The illustrative band energy potential diagram (**Fig. 2g**) shows both CB and VB (**Table S1**). The focus of this study is oxidation; and thus, we will analyze the VB position in more detail. The VB values display a volcano plot trend with the most positive value at 2.4 V vs. NHE for the 75M-25P composite, and 0.3 V than its counterparts 90M-10P and  $C_3N_4(M)$ . The samples with  $\geq 50\%$  purpald exhibited very similar values, *ca.* 1.5 V. Electronically speaking such result indicate that the 10-90% purpald content composites follow the VB position of  $C_3N_4(P)$  whilst for the high melamine content composites an enhanced composite was formed, exhibiting an increased potential (+0.2).

Theoretical water (1.23 V)<sup>[6,55]</sup> and benzylamine (0.95 V)<sup>[56,57]</sup> oxidation potentials (selected model reactions) were added in the diagram for discussion. All samples in principle can thermodynamically perform both oxidations, regardless of the over potentials involved. One can presume that the 75M-25P composite would undergo easier such oxidations due to its enhanced oxidation power, however the pre-requisites for undergoing oxidation is not limited to the VB edge position, since oxidation is a multi-step process of photo (physical and chemical) steps involved. To contextualize the obtained values for  $C_3N_4(M)$  and  $C_3N_4(P)$  of similar materials, one can compare with mesoporous  $C_3N_4$ , Fe-PHI, and K-PHI giving 1.82<sup>[36]</sup>, 2.70<sup>[58]</sup>, and 2.54<sup>[36]</sup> V vs. NHE, providing consistency and reliability of the present M-S measurements. Although the proton reduction is not at the core of this study, it can be said that according to the CB edges obtained (-0.1 - -0.5 V vs. NHE) all the resulting materials can theoretically enable such reduction. Though the over potentials and energetic barriers for this reaction are more significant than for the oxygen half reaction and therefore, may be difficult to perform.<sup>[59]</sup>

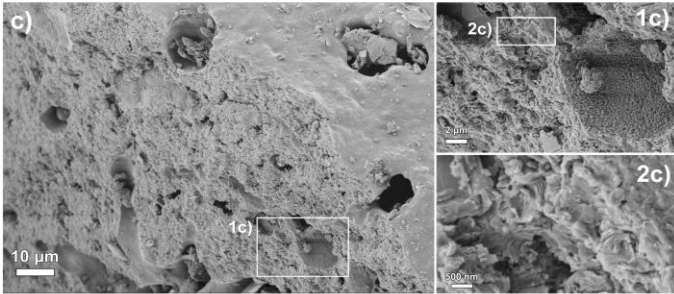
**90M-10P**



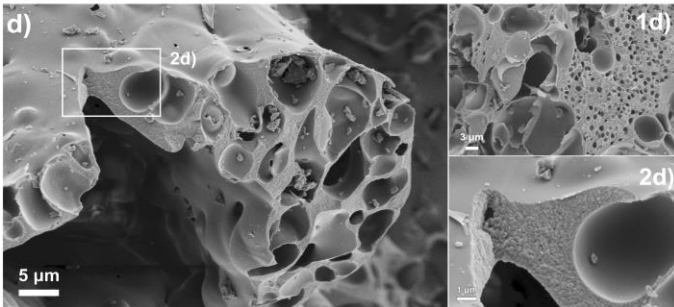
**75M-25P**



**50M-50P**



**25M-75P**



**10M-90P**

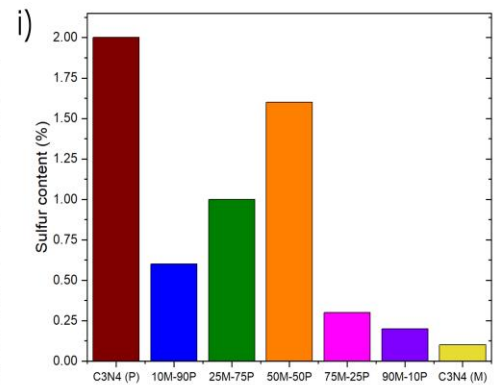
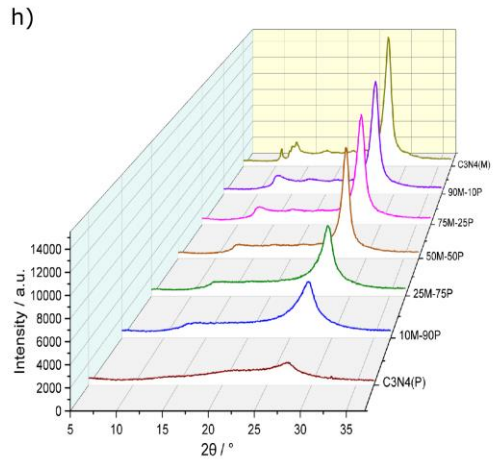
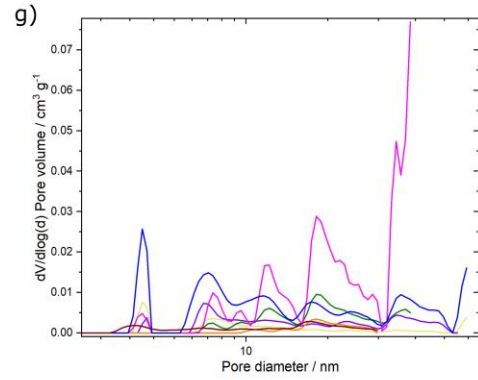
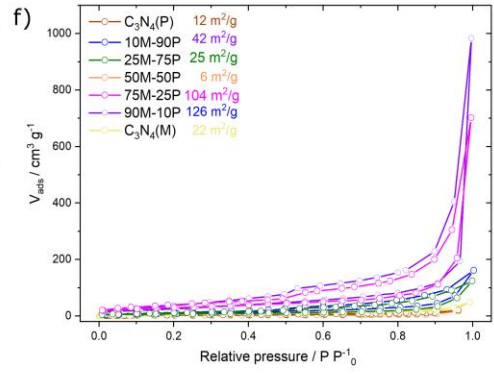
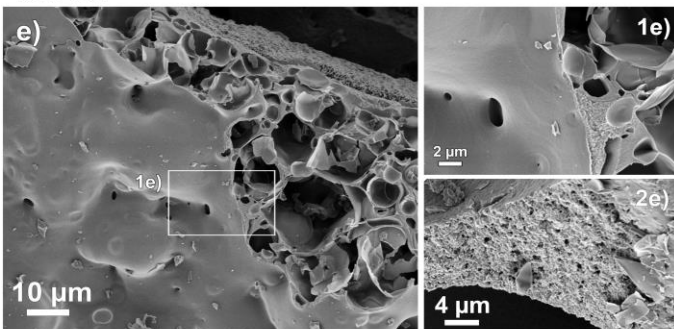


**Figure 3.** SEM images **a)** 90M-10P, **b)** 75M-25P, **c)** 50M-50P, **d)** 25M-75P, **e)** 10M-90P **f)** BET specific surface area, **g)** pore size distribution, **h)** XRD patterns, and **i)** sulfur content of all the as-prepared samples.

SEM images (**Fig. 3a-e and S3a-f**) reveal the morphologies of the five composites and  $C_3N_4(M \& P)$ . **Figure S3a-b** shows that  $C_3N_4(M)$  represents morphology of the layered materials, with align platelets oriented differently at the surface and inside the particles. A deeper look into the  $C_3N_4(P)$  reference can be found in **Figure S3c-f**. Grains possess large regions of flat surface and regions with spheroidal shape with some degree of surface roughness. Intriguingly, these spheroidal structures are presented in two forms: closed and open (dozens of micrometers). The spheroids are hollow, implying formation of gas bubbles, presumably due to the release of  $H_2S$  coming from the thiol functionality of the purpald precursor or a combination of  $H_2S$ ,  $N_2$ , and  $NH_3$  from the elimination mechanism.

The composites show a clear trend in their morphology in regard to the reference materials structure. 90M-10P and 75M-25P composites (**Fig. 3a-b**) showed stacking of flat layers, similar to the  $C_3N_4(M)$  sample, however with considerably more disorder in between layers and high number of pores. In addition, 90M-10P reveal some hollow tube shapes (stalagmite-like), with a potential reasonable explanation on how the material releases gases formed during thermal treatment. 10M-90P and 25M-75P (**Figures 3d-e**) consist of grains with smooth surface layers under which two types of morphologies are hidden: spheroid pore shapes as we observed in  $C_3N_4(P)$  incorporated into a more dense areas. The latter does not have any layered structure. In contrast the 50M-50P (**Fig. 3c**) sample has the most unique morphology among all. It consists of large grains with highly homogeneous smooth surface. The cross-sectional view on the grains shows densely packed layers, which however all together appeared much wavier when in 25M-75P. Large pores are present on the surface and the interior on the grains. Since the carbon nitrides references are morphologically very different, varying the purpald/melamine ratio leads to different combinations of these morphologies, with the 50M-50P making balance synergy. The self porogen effect (bubble signature as spheroid pore form) was essentially pronounced for the high purpald content ( $\geq 75\%$ ) samples. This porogen effect may be explained under two premises: a) purpald liquid solubility at 250 °C, entangling the melamine surface and b)  $H_2S$  elimination, driving different synergic effects at microstructural and morphological levels.

$N_2$  adsorption-desorption isotherms at 77K of all the samples in **Fig. 3f** show a combination of type-IV isotherm and type-H4 hysteresis loop. According to the IUPAC, this is ascribed to the presence of mesopores and slit-like pores in the samples.<sup>[60]</sup> The Brunauer–Emmett–Teller (*BET*) theory was used to calculate the specific surface area ( $S_{BET}$ ) of the materials. All the samples show low  $S_{BET}$  due to the very low adsorption at low relative pressures, except for 90M-10P and 75M-25P that show *ca.* 126 and 104  $m^2 g^{-1}$  (**Table 1**). QSDFT was used to obtain the pore size distribution of the samples (**Fig. 3g**). All of them show multimodal mesoporous profiles with pores ranging from 2 to 50 nm. 90M-10P stand out due to subtle differences in pore architecture – possessing the highest density of small-diameter pores ( $\sim 3$  nm). 50M-50P exhibited three pores between 10-16 nm close to the surface, with arbitrary depth (very low pore volume). The not well-defined pore size distribution of the samples is ascribed to the different mechanisms of  $C_3N_4$  phases formation, resulting in a range of mesopores cavities and depth combinations.

The XRD patterns (**Fig. 3h**) exhibited the typical diffraction peaks for  $C_3N_4$  at  $2\theta = 12.9^\circ$  &  $27.2^\circ$  for all the samples, corresponding to heptazine motif repetition and interlayer stacking of  $\pi$ -conjugated aromatic systems, respectively.<sup>[61]</sup> The latter is the 002 diffraction plane, characteristic for graphitic materials.<sup>[22,44,62]</sup> A qualitative study of the crystal size and  $d_{space}$  was performed to further exploit XRD data by understanding of the atomic layer disposition on the  $C_3N_4$  in-plane. Considering that the studied materials are heterogeneous, supported by SEM, this analysis is valid knowing that XRD is an average measurement of the heptazine unit repetition. Given those diffractogram positions and using peak fitting to obtain their Full Width Half Maximum (FWHM, **Fig. S4**), the  $d_{space}$  values were calculated using the Bragg equation at  $\sim 6.90 \text{ \AA}$  and  $\sim 3.36 \text{ \AA}$ , compared with the theoretical  $d_{space}$  values of a perfect  $C_3N_4$  with 7.13  $\text{ \AA}$  and 3.26  $\text{ \AA}$ . The reported decreased spacing between the repetitive heptazine units plus concomitant increase to interlayer stacking may be related to the inclusion of S atoms within the  $C_3N_4$ -skeleton causing firstly an expansion of the lattice and secondly

some in-plane tilt angularity, resulting in overall amorphicity.<sup>[63]</sup> The mean crystallite size (**Table 1**) calculated using the Debye-Scherrer relationship. The two largest crystallites were observed for the C<sub>3</sub>N<sub>4</sub>(M) (7.1±0.4 nm) and unexpectedly for the 50M-50P composite (7.2±0.4 nm). Once again, a volcano trend was found for crystallite size, indicating that at a ratio of 50M-50P the system is best compromised to preserve crystal size as of the C<sub>3</sub>N<sub>4</sub>(M) reference. As a general rule, larger crystallites are found in the composites with high melamine proportion ≥75%. In turn, smaller crystallite sizes are found for lower melamine content ≤25%. The smallest crystallite size was obtained for C<sub>3</sub>N<sub>4</sub>(P) with 1.8±0.4 nm, the most amorphous sample. This result implies that melamine load increases the crystal size while conversely, purpald content tunes the amorphicity of the obtained C<sub>3</sub>N<sub>4</sub>. One cannot exclude that purpald presence in the liquid phase solubilization or pyrolysis somehow inhibit the crystal growth, as has been observed in other S-doped/C<sub>3</sub>N<sub>4</sub> materials.<sup>[64]</sup> The number of layers (**Table 1**) in the stack followed the same volcano shape trend, with the largest number of layers obtained for the 50M-50P composite (21±1) plus C<sub>3</sub>N<sub>4</sub>(M, 21±1) samples, and the fewest layers in C<sub>3</sub>N<sub>4</sub>(P) (5±1), meaning that as the amorphous character increases, the material seems to be more exfoliated.

Elemental analysis was performed to determine the total sulfur, nitrogen, carbon, and hydrogen content (**Table S2**). The S content the composites again exhibited a volcano trend (**Fig. 3i**), excluding the highest S sample content, *ca.* C<sub>3</sub>N<sub>4</sub>(P) with ~2 wt. %. The second highest S content was found for the 50M-50P composite (1.6 wt. %), seemingly the optimal precursor ratio in preserving the S within the C<sub>3</sub>N<sub>4</sub> structural lattice. Such bulk S content respects the theoretical maximum amount of S (3.5 %) that a C<sub>3</sub>N<sub>4</sub> can host in relaxed geometric structure by first principles calculations considering one S atom per unit cell.<sup>[32]</sup> Further increasing purpald content (≥75%) in the C<sub>3</sub>N<sub>4</sub> composites, induces a decrease in S content ranging between 0.6 and 1% whilst the low purpald (≤25%) C<sub>3</sub>N<sub>4</sub> composites and the C<sub>3</sub>N<sub>4</sub>(M) reference present very low amount of S (≤0.3 %), almost at trace scale.

Nitrogen content varies marginally by ±3.9 %, implying a plausible substitution of N by S atoms. For nitrogen content purposes, the samples are divided in three groups. The first consists of low purpald content (≤25%) plus C<sub>3</sub>N<sub>4</sub>(M) giving 62.3 % of N on average, then we have separated the exceptional 50M-50P composite (61.3 % N), and finally grouped the high purpald content (≥75%) of 58.9% average N. The latter trend indicates that if the purpald (S-container) content increases in the mix, the lower the nitrogen content, indicating a clear atomic substitution. For carbon, changing synthetic parameters results in a less significant variation than for N values. However, the samples can nonetheless be divided in high, intermediate, and low content as follows: 0.25, 50-90, and 100 % of purpald, respectively. One cannot omit the possibility of C substitution by S atoms, if this hypothesis is indeed accurate, it will be true to a lower extent compared to N substitution, supported by the EA results. The C/N ratio for all samples was around ~0.56, which is lower than the perfect C<sub>3</sub>N<sub>4</sub> (0.64),<sup>[21,44]</sup> suggesting incomplete condensation presumably due to the first thermal step that quenches/accelerates the sublimation simultaneously. In the same incomplete condensation context, the H content remains constant (2%), proof of equal quantity of terminal amines for all the samples.

**Table 1.** Specific surface area, pore size/volume, mean crystallite size, number of layers, sulfur content in the bulk, and C/N ratio of the as-prepared materials.

| Sample                            | S <sub>BET</sub><br>m <sup>2</sup> g <sup>-1</sup> | Crystallite<br>nm | Layers *<br>N° | S bulk<br>wt.% |
|-----------------------------------|--|-------------------|----------------|----------------|
| C <sub>3</sub> N <sub>4</sub> (P) | 12±1   | 1.8±0.4           | 5±1            | 2.0±0.2        |
| 10M-90P                           | 42±4   | 2.4±0.4           | 7±1            | 0.6±0.1        |
| 25M-75P                           | 25±3   | 3.5±0.4           | 11±1           | 1.0±0.2        |
| 50M-50P                           | 6±1  | 7.2±0.4           | 21±1           | 1.6±0.2        |
| 75M-25P                           | 104±10   | 6.2±0.4           | 18±1           | 0.3±0.1        |
| 90M-10P                           | 126±13   | 6.5±0.4           | 19±1           | 0.2±0.1        |
| C <sub>3</sub> N <sub>4</sub> (M) | 22±2   | 7.1±0.4           | 21±1           | 0.1±0.1        |

\* = calculated as described by Saner et al.<sup>[65]</sup>

The FT-IR spectra (**Fig. S5**) of all samples exhibited the same characteristics peaks of  $C_3N_4$ .<sup>[43]</sup> The broad absorption band ( $2900 - 3350\text{ cm}^{-1}$ ) was assigned to the N-H stretching vibration of secondary (C-NH-C bridge bond along the repeating motif phases) and primary amines (the terminating edge layer, C-NH<sub>2</sub>).<sup>[42]</sup> One can also attribute them, to a lesser extent, to the hydroxyl O-H stretching due to the adsorbed water species.<sup>[66]</sup> The defined sharp peaks in the range  $1620$  to  $1230\text{ cm}^{-1}$  were ascribed to the fingerprint of heptazine units. A detailed explanation of the attribution of the different peaks was reported by Jimenéz *et al.*<sup>[43]</sup> Two additional sharp bands were present ( $800$  and  $890\text{ cm}^{-1}$ ) and attributed to N-H deformation mode and heptazine ring breathing mode.<sup>[42]</sup> In conclusion, all the 7 samples showed the characteristic  $C_3N_4$  peaks and are consistent with literature.<sup>[67]</sup>

### 2.3. Photooxidation performance

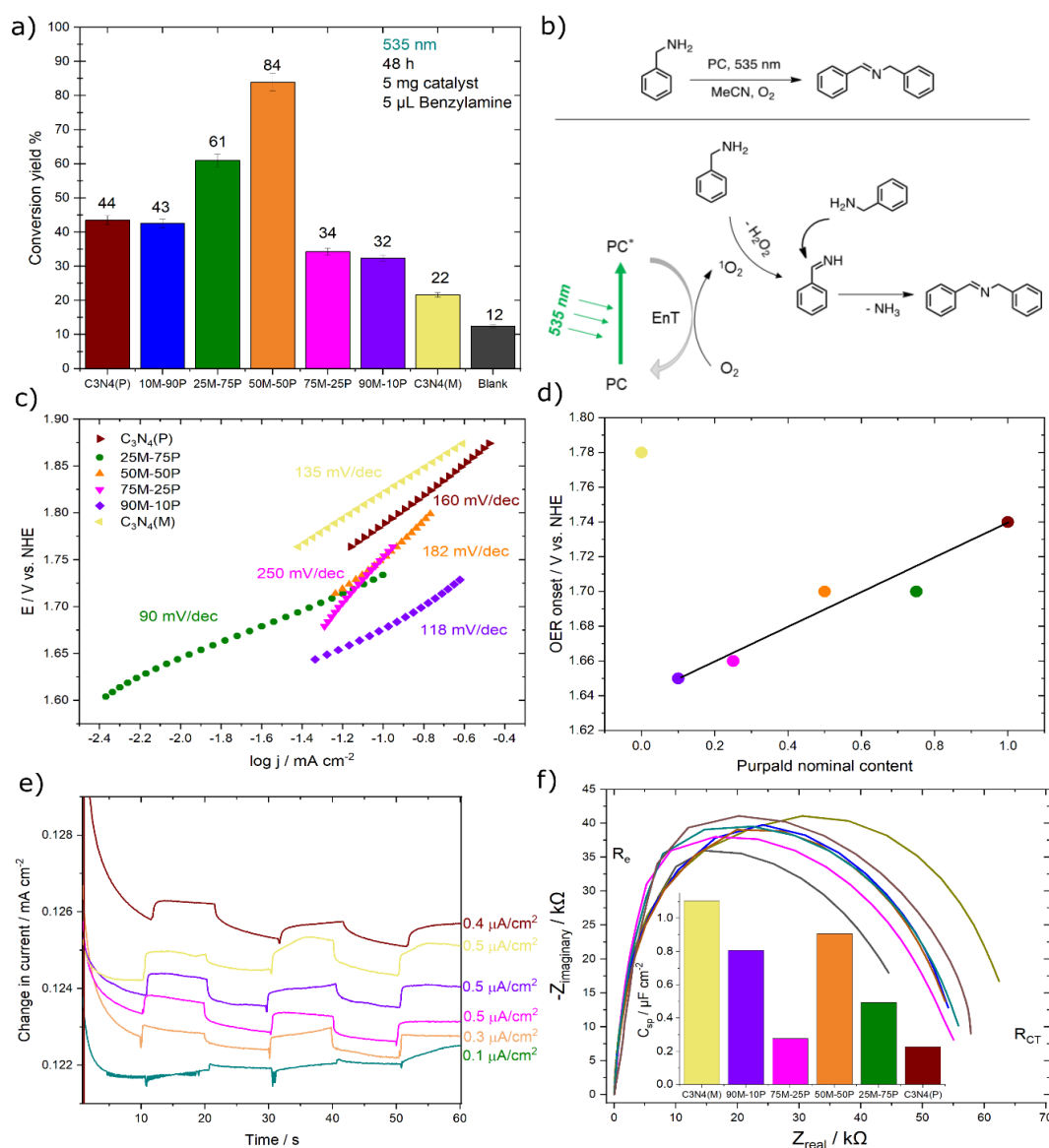


**Figure 4.** **a)** Photooxidation of benzylamine including the reaction conditions, **b)** illustrative mechanism and species involve in the photo conversion of benzylamine to dibenzylimine, **c)** Tafel slopes for OER reaction, **d)** purpald content in function of OER onset values **e)** on-off CA curves recorded using a white LED lamp, and **f)** Nyquist plot of all the materials.

The photooxidation conversion of benzylamine (substrate) to dibenzylimine was studied (**Fig. 4a**), upon monochromatic green light irradiation at 535 nm to excite (Emission spectra, **Fig. S6**)  $C_3N_4$  materials, which is unusual, unless they have a great portion of visible light absorption. Figure 4 illustrates the volcano trend found for the series of the as-prepared materials. Here, the 50M-50P

composite exhibited the highest conversion yield of  $84\pm 3\%$ , establishing it the most active material of the series followed by 25M-75P with 61% conversion yield. The remaining samples have diminished conversion yields in the order of 1, 2, and 3-fold lower, for  $C_3N_4(P)/10M-90P$ , 90M-10P/75M-25P, and  $C_3N_4(M)$ , respectively. It is imperative to mention that a blank (experiment without catalyst) conducted to account the contribution of photolysis (light) or thermolysis (temperature), determined to be 12% yield, almost the half the capacity of the least active sample.

Photocatalytic benzylamine oxidation may proceed via two mechanisms that may also combined. First, through electron transfer to the oxygen and by forming an oxygen radical-anion species and second, through energy transfer to the oxygen, forming a singlet oxygen.<sup>[68]</sup> Both reactive species can take part in the subsequent oxidation of benzylamine. To evaluate the more plausible mechanism in our case, an EPR investigation was carried out. **Fig. S7** shows that both species might be potentially formed over the 50M-50P composite. However, with respect to the previous studies,<sup>[52,69]</sup> we assume that the energy transfer mechanism is dominant upon 535 nm irradiation, as this low energy input was earlier shown to be not sufficient to induce electron transfer to  $O_2$ . The mechanism is sketched in **Fig. 4b**.

#### 2.4. Photoelectrochemical performance

The oxygen evolution reaction (OER) was studied using the as-prepared  $C_3N_4$  materials as catalysts in alkaline media. **Fig. S8** shows the linear sweep voltammetry curves, exhibiting similar catalytic activity with close onset potentials. The onset potentials are plotted against the purpald nominal ratio in **Figure 5d**, showing that the composite materials perform better than the two  $C_3N_4(M \& P)$  references given their lower values ( $\leq 1.70$  V vs. NHE). The composites' onset potentials show a linear increase with increasing purpald content. Interestingly, the lowest onset is observed for the composite with only 10 wt. % of purpald. The Tafel slopes (**Fig. 5c**) exhibit a non-linear trend as a function of the precursor nominal ratio. The photoresponse of the materials (**Fig. 5e**) was measured at a bias of 0.6 V vs. Ag/AgCl with a white LED lamp (Emission spectra, **Fig. S9**). The samples exhibit similar photoresponse except for 25M-75P, showing negligible photoresponse probably due to fast charge carrier recombination. The observed samples photoresponse are forward bias, typical for n-type SC.<sup>[16]</sup>

Mott-Schottky curves and flat band potential diagram (**Fig. 2f and 2g**) show that the VB and CB positions for all samples lie within the value needed for OER. The differences in onset potential follow the conductivities of the samples.  $C_3N_4(M)$  has the highest charge transfer resistance, resulting in the highest onset potential (1.78 V vs. NHE). The charge transfer conductivity of the composites follows the trend of the obtained onset potentials, excluding 90M-10P. Therefore, one can conclude that the value of the onset potential is mostly influenced by the conductivity of the sample for these specific materials. The best performing sample 90M-10P has the highest surface area ( $126 \text{ m}^2 \text{ g}^{-1}$ ), therefore the high performance is likely correlated to the accessibility to the catalytic active sites.<sup>[70]</sup> Yet, the conductivity of a SC is not trivial to understand and may be influenced by many factors, *e.g.*, particle size, grain boundaries, crystallinity, heteroatom doping, wettability, among others.<sup>[71]</sup>

The present  $C_3N_4$  materials' onset potentials are in the same range typically obtained for  $C_3N_4$  with transition metals or hybrids  $C_3N_4$  with heteroatom doping. Whilst the obtained Tafel slopes are high, the resulting materials exhibit slower performances than other reports, see **Table S3**. A previous reported S-doped/ $C_3N_4$  exhibited 1.42 V vs. RHE onset, even lower than all the studied samples. However, its Tafel slope ( $120 \text{ mV/dec}^{[72]}$ ) is among the highest values in literature and slightly lower than the ones reported in this study. We assume that the introduced sulfur atoms in the  $C_3N_4$  skeleton result in a more hydrophobic surface. This hydrophobicity may hinder the proximity of reactants to the  $C_3N_4$  vicinity, disabling an effective oxidation of water by lowering the adsorption rate.<sup>[73]</sup>

**Figure 5f** displays the Nyquist plot and the values of specific capacitance. The electrode resistance is relatively low for all the samples, implying good interface contact of the material and electrode

support. The charge transfer resistance of the composites (*ca.* 60 k $\Omega$ ) is lower than the two C<sub>3</sub>N<sub>4</sub>(M & P) references, though similar among themselves. The pure C<sub>3</sub>N<sub>4</sub>(M) shows the highest specific capacitance (1.1  $\mu\text{F cm}^{-2}$ ). Surprisingly, the 50M-50P sample has the second highest specific capacitance (0.9  $\mu\text{F cm}^{-2}$ ) particularly close to the highest, although with four-fold lower surface area than C<sub>3</sub>N<sub>4</sub>(M). The high capacitance of C<sub>3</sub>N<sub>4</sub>(M) and 50M-50P likely comes from the large crystal size, associated with the long atomic arrangement in the C<sub>3</sub>N<sub>4</sub> skeleton that enhances the conductivity. Considering the specific capacitance differences of 90M-10P and 50M-50P compared to C<sub>3</sub>N<sub>4</sub>(P), this work implies that these composites may allow new design of metal-free capacitors by improving them with additional modifications via functionalization or vacancies creations, etc.

## 2.5. Advanced characterization and correlations

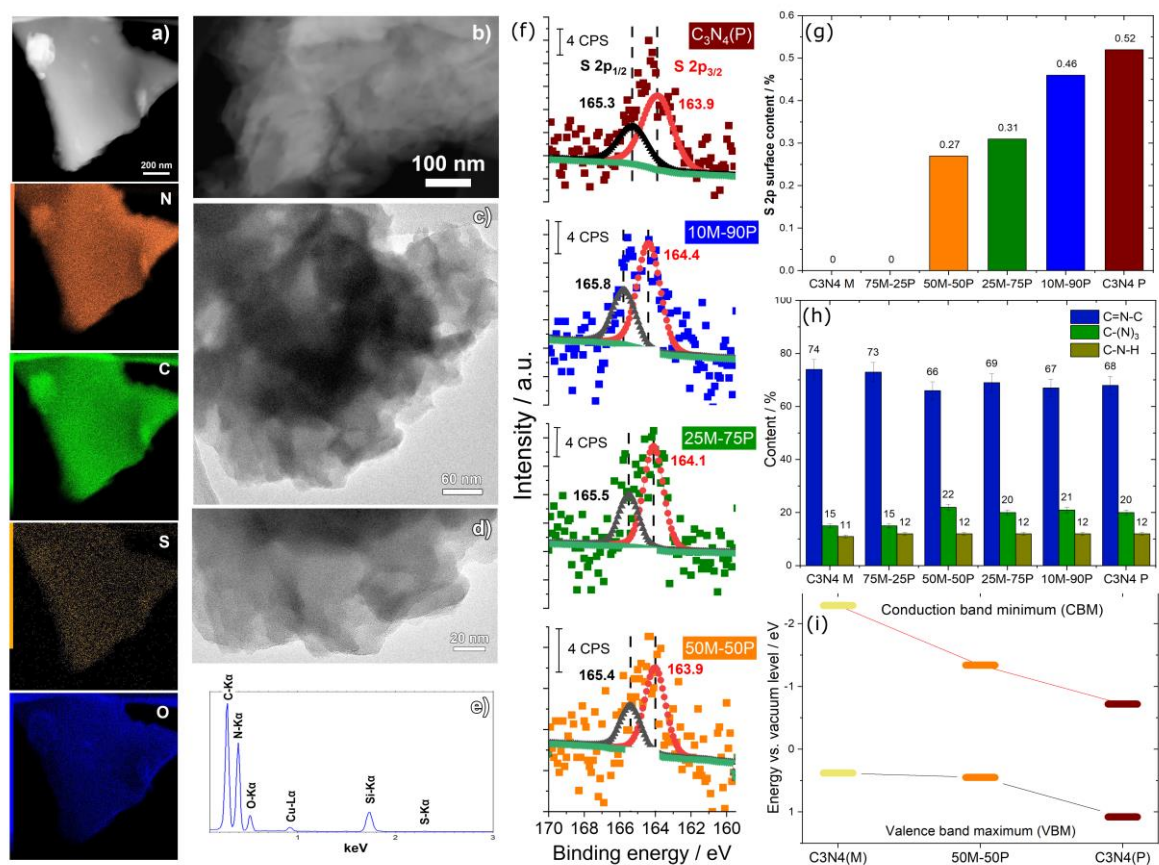


**Figure 5.** a) EDX element mapping distribution of 50M-50P composite, b) HAADF, c-d) HRTEM of 50M-50P composite, e) EDX associated spectra, f) XPS S 2p spectra of the materials. Summary of the amount of g) sulfur (S2p XPS signal) and h) the different amounts of nitrogen functionalities (components of the deconvolution of the N1s XPS signal) obtained from XPS analysis. i) Energy band alignment diagram obtained from UPS results.

EDX elemental maps and the corresponding spectrum of the most photoactive 50M-50P composite (Fig. 5a and 5e) confirmed the presence of N, C, S, and O atoms in the sample, homogeneously distributed on the surface. The lower presence of O can be explained through physically adsorbed O<sub>2</sub>.<sup>[74]</sup> The S content is the lowest signal as expected, since it is in a very low amounts (1.6 wt. % by EA). As suggested by DFT calculation, the S-doping is preferentially oriented to substitute the sp<sup>2</sup> nitrogen of the tri-s-triazine unit for geometric relaxation aspects.<sup>[33]</sup> The homogeneous S distribution along the grain surface points to its well-distributed doping coverage. Interestingly, the same homogeneous distribution of S, N, C, and O were found for the C<sub>3</sub>N<sub>4</sub>(P) (Figures S10 and S11).

To compare materials at the nanoscale we performed high-resolution transmission electron microscopy (HRTEM) and annular dark-field scanning transmission electron microscopy (HAADF) and bright

field analysis of the two references and 50M-50P composite. By HAADF comparison (**Fig. 5b** and **S12 a/d**), a linear trend was found on brightness ranging from the brightest  $C_3N_4(P)$  towards the darker  $C_3N_4(M)$ , due to the S content. HRTEM images (**Figs. 5c-d**, **S12b-c**, and **S12e-f**) revealed typical  $C_3N_4$  lamellar texture, 2D interconnected layer morphology, the edges appeared symmetrical to some extent, and the hexagonal arrangement of the heptazine scaffolding units is noticeable. Interestingly,  $C_3N_4(P)$  material (**Fig. 5c-d**), exhibits a more transparent domain, composed of a stack of well-distributed layers and thus a thin or exfoliated stacked in agreement with XRD small crystallite size and a few layers. The 50M-50P (**Fig. 5c-d**) and  $C_3N_4(M)$ , (**Fig. S12 d-f**) materials show a darker image contrast, potentially due to two effects: a) thicker stacks of layers compared to  $C_3N_4(P)$  and b) the layers are not homogeneously superposed between each other, given a non-symmetrical entanglement.

Surface analysis of the obtained  $C_3N_4$  materials was performed using X-ray photoelectron spectroscopy, to elucidate the atomic bonding in the  $C_3N_4$  skeleton and probe their local chemistry. XPS analysis will focus on the peaks of N 1s (400 eV), C 1s (285 eV), and S 2p (165 eV) that were fitted using modified Voigt-type line shapes. The high-resolution XPS S 2p signal (**Fig. 5f**) displays the single spin-orbit doublet peak at *ca.* 164 and 165 eV positions, ascribed as the S 2p<sub>3/2</sub> and S 2p<sub>1/2</sub> doublet of C-S type sulfur, consistent with literature.<sup>[31,32,34,35,72,75,76]</sup> The 164 eV peak evidences the partial substitution of hybridized N by S atoms in the lattice.<sup>[75]</sup> This finding is consistent with DFT calculations that revealed that the substitutional S atoms doping preferred to substitute the N over the C, for geometric preservation in relaxed heptazine units.<sup>[33]</sup>

**Fig. S13a** displays deconvoluted N1s XPS spectra of the samples. The signals are deconvoluted in three well-resolved peaks at 398.6 (most intense), 399.8, and 401.0 eV, ascribed as the sp<sup>2</sup> hybridized pyridine N from heterocyclic aromatic rings (C=N-C bonds), tertiary bridges (N-C<sub>3</sub>), and amino groups (C-N-H).<sup>[43,55,77-79]</sup> **Fig. S13b** exhibits the classic three peaks of C at 284.8, 285.9, and the dominant peak at 288.3 eV. The 284.8 eV was assigned as adventitious carbon (C-C) or sp<sup>3</sup> defects on the edge of graphitic domains or potentially as C-S bonds. Then 285.9 and 288.3 eV were assigned to the C-O as for adsorbed O<sub>2</sub> species, supported by EDX, and sp<sup>2</sup> coordinated N=C-(N)<sub>2</sub> from the heterocyclic ring.<sup>[43,77-79]</sup> Interestingly, S 2p and N 1s signals of the composites shifted slightly towards higher binding energies as purpald load increases, indicating that the S-doping induced changes in the surface electronic  $C_3N_4$  structure as previously seen by Wang et al.<sup>[31]</sup>

Regarding the quantitative XPS analysis of S 2p (**Fig. 5g**). The S amount has a linear increase while S-doping/purpald increases. Nevertheless, these surface quantities are 3-5-fold lower than the bulk obtained by EA. This trend suggests that the incorporated S atoms in the  $C_3N_4$  skeleton are partially embedded and partially in the surface. For the bulk S atoms may be accessible by the porous channels, whilst for the surface S atoms are exposed for immediate surface reactions. **Fig. 5h** displays the sp<sup>2</sup> pyridine N content remains constant until 25% purpald, and then decreases at contents of 50% and above, consistent with the increase of N atoms substitution by S. Since, the bridging tertiary N remains constant for the composites ( $\geq 50\%$ ) and  $C_3N_4(P)$ , no drastic changes in the interconnected heptazines may be inferred. However, a lower proportion of this tertiary N was found for  $C_3N_4(M)$  and 75M-25P, presumably due to non-symmetric atomic arrangements in the x or y axis of the heptazine direction. The amino groups are constant in the surface for all the samples in agreement with H content by EA.

**Fig. S13c** shows the sp<sup>2</sup> C of the 50M-50P composite exhibits a higher content compared to its homologues, reinforcing the previously established hypothesis that the S substitution occurs mainly on the N rather than C. For the superposed C-S signal with adventitious C, 50M-50P and  $C_3N_4(P)$  have the highest value (20-24 %), correlated to bulk S content. No differences were found for the C-O content among the samples, indicating that they probably adsorb the same quantity of O<sub>2</sub> species.

The energy band alignment diagram (**Fig. 5i**) was constructed from UPS results (**Fig. S14a**) and serves to determine how the S doping and defects contribute to the electronic modulation of the most photoactive 50M-50P composite relative its two references. Theoretically, an S impurities are

considered as anionic doping to substitute a majority of N atoms.<sup>[80]</sup> The valence band maximum (VBM) of 50M-50P position is very similar than C<sub>3</sub>N<sub>4</sub>(M), emphasizing little change despite the 50-50 initial mix of precursors, the composite preserves the electronic character of such reference. Nonetheless one cannot neglect the possibility of intra band states formation near to the VBM, due to the upward increase compared to C<sub>3</sub>N<sub>4</sub>(P). Interestingly, the C<sub>3</sub>N<sub>4</sub>(P) has the most positive VBM of all (1.1 eV), suggesting a high capacity to undergo oxidations.

Looking at the conduction band minimum (CBM) of 50M-50P is shifted toward positive and negative energy in reference to C<sub>3</sub>N<sub>4</sub>(P) and C<sub>3</sub>N<sub>4</sub>(M), giving a new intermediate hybrid CBM energy position. This new position may be explained by considering the synergistic effect of both precursors, and the successful S insertion, presumably promoting the S 2p orbitals interacting with the 2p of C from the  $\pi$ -conjugated system or by the deep structural defects cause by the distorted lattice.<sup>[32,36,53]</sup>

**Fig. S14b** displays the work function (WF) values of C<sub>3</sub>N<sub>4</sub>(M), C<sub>3</sub>N<sub>4</sub>(M), and 50M-50P, calculated from a calibrated Fermi level with an internal gold reference. The resulting WF were 4.0, 3.1, and 3.2 eV, respectively. Considering that the theoretical WF of C<sub>3</sub>N<sub>4</sub> is 4.65 eV<sup>[81]</sup>, one can notice that the experimental value of C<sub>3</sub>N<sub>4</sub>(M) is similar. The difference of the other two samples, however, varies significantly (*ca.* 1.55 eV) potentially due to their amorphous nature. The present solid-state reaction comprehends two stationary temperatures, differing from the typical mesoporous or polymeric carbon nitride (single thermal treatment), modulating C<sub>3</sub>N<sub>4</sub> structural, geometric, electronic, and optical properties, thus WF differences were expected.

### 3. Conclusions

A series of S-doped/C<sub>3</sub>N<sub>4</sub>-based materials were synthesized demonstrating enhanced optical, electronic, structural, geometric, textural, and morphological properties than their C<sub>3</sub>N<sub>4</sub> references. The composites exhibited higher performance in benzylamine photooxidation, oxygen evolution, and in storing energy (capacitor brief investigation) than references. Thus, this work serves to continue improving amorphous catalysts with long-visible-light range for solar energy conversion and storage.

The 50M-50P composite exhibited the highest photooxidation organic conversion yield (84±3%) of benzylamine to dibenzylimine in O<sub>2</sub> atm upon green monochromatic light (535 nm) in 48h. This result is attributed to the discrete shoulder in the visible light range (~700 nm edge), the unusual high sulfur content (1.6 wt. %) for a carbonaceous material, the homogeneous sulfur doping along its surface by substituting preferentially N atoms in the heterocycle, low porosity nature, new intra band energy states, preservation of crystal size, thick sheet stacking, rare deep structural defects due to layer distortion, flat surface morphology with a sharp roughness, hydrophobic surface, and 10-16 nm pores.

## 4. Experimental section

### 4.1. Materials

4-amino-3-hydrazino-5-mercapto-1,2,4-triazole or commercially called purpald (C<sub>2</sub>H<sub>6</sub>N<sub>6</sub>S, ≥99%, Sigma Aldrich), melamine (C<sub>3</sub>H<sub>6</sub>N<sub>6</sub>, 99%, Sigma Aldrich), ethanol (≥99%, Sigma Aldrich), potassium hydroxide (KOH, Alfa Aesar), Nafion (15-20% water, 1100W, Sigma Aldrich), acetonitrile (CH<sub>3</sub>CN, Supelco, hypergrade for LC-MS), benzylamine (99%, Sigma Aldrich) were used without further purification.

### 4.2. Synthesis of C<sub>3</sub>N<sub>4</sub> Materials

Graphitic carbon nitride references, initiated with either melamine or purpald alone, and C<sub>3</sub>N<sub>4</sub> composites were synthesized via thermal polycondensation under continuous N<sub>2</sub> flow. The one-pot solid-state thermal polycondensation reaction was carried out in a static furnace applying a heating ramp of 1.9 °C min<sup>-1</sup> until reach 250 °C and keeping it constant for 2h and a second ramp of 1.7 °C min<sup>-1</sup> and keeping it constant at 550 for 2h in a continuous N<sub>2</sub> of 1 bar. For the C<sub>3</sub>N<sub>4</sub> composites a

variation of the ratio of the two precursors (ranging from 10, 25, 50, to 75 wt. %) were put into an alumina crucible with a lid respecting the established mass ratio. For simplicity, the C<sub>3</sub>N<sub>4</sub> composites are described as with the initial mass ratio used, *e.g.*, 10M-90P, where M stands for melamine (10 wt. %) and P for purpald (90 wt. %).

### 4.3. Preparation of Electrodes

The working electrode's preparation consist in several steps. First, F-doped tin oxide (FTO) glass is pretreated, through cleaned by sonication in ethanol for 30 min and oven drying at 80°C. The defined area of 0.25 cm<sup>2</sup> of the FTO glass was protected using Scotch tape. Secondly, 3 mg of each material were weighted in a vial and 20 µL of Nafion (binder) and 0.2 mL of ethanol were added. This slurry was stirred overnight, then sonicated for 15 min and 25 µL of the suspension was deposited by drop casting onto the pretreated FTO coated glass electrode (area 0.25 cm<sup>2</sup>). Finally, the electrode was air-dried at room temperature for half a day, the Scotch tape was removed and further dried at 120°C for 2h under continuous flow of Argon to improve adhesion.

### 4.4. Materials Characterization

Thermogravimetric analysis (TGA) was performed using a NETZSCH TG 209 F1 device. Each sample was placed into a platinum crucible and heated from room temperature (*ca.* 25 °C) up to 1000 °C with a heating rate of 10 °C min<sup>-1</sup> under nitrogen flow of 20 mL min<sup>-1</sup>. The standard deviation of the decomposition temperature of the analysed samples is ±10 °C.

TGA-MS measurement was performed using a thermo microbalance TG 209 F1 Libra (Netzsch, Selb, Germany) coupled with a Thermostar Mass spectrometer (Pfeiffer Vacuum; Asslar/Germany) with an ionization energy of 75 eV. A platinum crucible was used for the measurement of 10 ± 1 mg of samples in a Helium flow of 10 mL min<sup>-1</sup> and a purge flow of 10 mL min<sup>-1</sup>. The samples have been heated with heat rate 2.5 K min<sup>-1</sup> to 910 °C. Data have been recorded and analysed by the Proteus (6.1.0) and Quadstar-software package (7.03, MID modus).

UV-vis-NIR absorption spectra were recorded on an Agilent Cary 5000 UV-Vis-NIR spectrophotometer equipped with a diffuse reflectance-integrating sphere. The acquiring starting and ending wavelengths were 300 until 1000 nm, with a scan time of 0.1, data interval of 1, and scan rate of 600 nm min<sup>-1</sup>. The bandgap was calculated by a statistically representative linear fit of the tangent decay curve (1–4 eV) by Tauc plot.

Steady-state emission spectra ( $\lambda_{\text{ex}}= 365$  nm) were recorded using an FLS980 photoluminescence spectrometer (Edinburgh Instruments Ltd, the United Kingdom) equipped with an ozone-free Xenon arc lamp as the light source in a powder holder. Transient photoluminescence ( $\lambda_{\text{ex}}= 375$  nm laser source) spectra were recorded using a PicoQuant FluoTime 250 fluorescence spectrometer equipped with PicoQuant PDL 820 picosecond diode laser controller. The experimental settings were: 10000 counts, 25 ps resolution, 40 MHz frequency, 54.7 ° Polarizer, 1 nm excitation band width. The decay profiles were fitted using a multiexponential decay model and  $\tau$  (average lifetime) of the charge carriers is reported following an existing methodology,<sup>[82]</sup> fitting was done using Tau 2 software.

Elemental analysis (EA) by combustion was accomplished using a Vario Micro device.

Scanning electron microscopy measurements were performed using a Zeiss Leo 1550 equipped with field emission gun and an Oxford Instruments energy-dispersive X-ray detector X-MAX (80mm<sup>2</sup>). Secondary electron images were recorded at 3kV using an Everhart–Thornley detector.

Nitrogen adsorption/desorption isotherms were performed in a Quantachrome Quadrasorb SI-MP porosimeter at 77.4 K. The samples were degassed prior to the measurements at 150 °C under vacuum (0.5 Torr) for 20 h in a 3 P Instruments Masterprep degassing machine. The Brunauer-Emmett-Teller (BET) model was applied to the adsorption isotherm to calculate the specific surface area from the

data ( $0.05 < P/P_0 < 0.2$ ) using the QuadraWin 5.05. The total pore volume (VT) was calculated from the amount of gas adsorbed at  $P/P_0 = 0.995$ . The pore size distribution was calculated by using a quenched solid density functional theory (QSDFT) model with a slit/cylindrical pore shape using the nitrogen adsorption data.

XRD measurements were carried out with a Rigaku Smart-Lab X-ray diffractometer equipped with a D/tex Ultra250 detector with Cu K alpha1 radiation ( $\lambda = 1.5418 \text{ \AA}$ ) and Johansson monochromator. The scanning was performed at  $2\theta$ - $\theta$  mode, ranging from 5 to 40°, step size of 0.05, and speed of 2 °/min. Prior to scanning, the powders were inserted into an aluminum sampler holder with a diameter and depth of 2.4 x 0.2 cm. Before each measurement an optical and sample alignment were carried out to guarantee the best signal/noise ratio. The divergence slit was calculated through virtual crystallographic calculators V.2 from UCL, knowing the sample length (2.4 cm), lowest angle (5°) and the goniometer radius (30 cm). Beam stop and scattering slit plate were used to suppress background and avoid scattering interference signals. Fitting the XRD patterns was performed through Voigt method in Origin 2021b to calculate the Full Width Half Maximum (FWHM) and the position to apply the Bragg law and Debye-Scherrer equations to get  $d_{\text{space}}$  and crystallite size values of all the series.

Fourier transform infrared attenuated total reflectance (FTIR-ATR) spectra were recorded with a Thermo Fisher Nicolet iS5 spectrometer equipped with an attenuated total reflection unit of diamond. Measurements were acquired in the 750–3700  $\text{cm}^{-1}$  range with 32 scans and 8  $\text{cm}^{-1}$  of resolution. The characteristic doublet of the atmospheric  $\text{CO}_2$  2340/2360  $\text{cm}^{-1}$  signal could not be removed from the spectra after background subtraction due to physisorbed  $\text{CO}_2$ .

The Mott-Schottky measurements were performed in a Gamry Interface 1000 potentiostat using a 3-electrode cell. Such cell consists of a Pt wire as a counter electrode, Ag/AgCl as a reference electrode, and FTO glass coated with the material as working electrode. Aqueous solution of KOH (0.1 M) was used as an electrolyte and all the measurements were done at ambient temperature. The acquisition conditions of the samples comprised the potential range from -2 V to 1.2 V RHE, 0.05 V potential step, and frequencies from 10 KHz to 100 Hz, 10 mV potential amplitude.

XPS data was acquired using a Kratos Axis SUPRA using monochromated Al K $\alpha$  (1486.69 eV) X-rays at 15 mA emission and 12 kV HT (180W) and a spot size/analysis area of 700 x 300  $\mu\text{m}$ . The instrument was calibrated to gold metal Au 4f (83.95 eV) and the dispersion adjusted to give a BE of 932.6 eV for the Cu 2p $_{3/2}$  line of metallic copper. The Ag 3d $_{5/2}$  line FWHM at 10 eV pass energy was 0.544 eV. The source resolution for monochromatic Al K $\alpha$  X-rays is  $\sim 0.3$  eV. The instrumental resolution was determined to be 0.29 eV at 10 eV pass energy using the Fermi edge of the valence band for metallic silver. Resolution with charge compensation system on was  $< 1.33$  eV FWHM on PTFE. High resolution spectra were obtained using a pass energy of 20 eV, step size of 0.1 eV and sweep time of 60s, resulting in a line width of 0.696 eV for Au 4f $_{7/2}$ . Survey spectra were obtained using a pass energy of 160 eV. Charge neutralisation was achieved using an electron flood gun with filament current = 0.4 A, charge balance = 2 V, filament bias = 4.2 V. Successful neutralisation was judged by analysing the C 1s region wherein a sharp peak with no lower BE structure was obtained. Spectra have been charge corrected to the main line of the carbon 1s spectrum (adventitious carbon) set to 284.8 eV. All data was recorded at a base pressure of below  $9 \times 10^{-9}$  Torr and a room temperature of 294 K. Data was analysed using CasaXPS v2.3.19PR1.0. Peaks were fit with a Shirley background prior to component analysis.

The UV source is a UVS 10/35 helium discharge lamp (SPECS), which supplied He(I) radiation @ 21.22 eV. For UPS, a system with a hemispherical electron analyser (CLAM 4 by VG) and an electron detector of 9 discrete channeltrons was operated at 5 eV pass energy. The angle between UV source and entrance cone of the analyser is 54° with the electron lens placed perpendicular to the probed surface. A sputter-clean Au foil served as reference sample to determine the position of the Fermi edge. The sample was kept at -15 V vs. ground to accelerate the emitted electrons towards the

analyser. For transmission electron microscopy (TEM) observations, a suspension of the sample in ethanol was sonicated for 10 minutes and then drop-casted to the Cu grid with a lacey carbon support and dried for 15 minutes. The TEM study was performed using a JEOL JEM-F200 (S) TEM operated at 80kV and equipped with a field emission gun and a high-angle silicon drift Energy Dispersive X-ray (EDX) detector (solid angle up to 0.98 steradians with a detection area of 100 mm<sup>2</sup>). TEM images were recorded using TVIPS TemCam-F216. Annular Dark Field Scanning Transmission Electron Microscopy (ADF-STEM) images were collected at a probe convergence semi-angle of 25mrad.

EPR measurement were conducted on a Bruker EMXnano benchtop X-Band EPR spectrometer. The following settings have been used for all spectra acquisition unless other is specified: Center Field 3444.05 G, Sweep Width 200 G, Receiver Gain 60 dB, Modulation Amplitude 1.000 G, Number of Scans 4, Microwave Attenuation 10 dB. Sample were placed and flame-sealed in EPR capillaries (IntraMark, volume 50  $\mu$ L, ID 0.86 mm), inside EPR tubes (ID 3 mm, OD 4 mm, length 250 mm). In-situ EPR measurements of photocatalytic experiments have been performed coupling Thorlabs M415F3 Fiber-Coupled LED (64 mW $\cdot$ cm<sup>-2</sup> measured at 0 cm distance) with Thorlabs DC2200 High-Power LED controller.

#### Photocatalytic TEMPO detection experiment

A solution of 2,2,6,6-tetramethylpiperidine (TEMP) (5  $\mu$ L, 0.03 mmol) in CH<sub>3</sub>CN (3 mL) was prepared in a 4 mL glass vial. The solution was flushed via the double needle technique with O<sub>2</sub> for 2 minutes. The most active catalyst (50M-50P) was prepared under the same reaction conditions, and it was introduced into a capillary (IntraMark, volume 50  $\mu$ L, purchased from BRAND GMBH + CO KG) was sealed in the flame of gas burner from one side. The capillary was charged with an aliquot of the TEMP solution in CH<sub>3</sub>CN (20  $\mu$ L, 0.01 mol $\cdot$ L<sup>-1</sup>). The open end of the capillary was sealed in the flame of a gas burner and placed into an EPR tube (ID 3 mm, OD 4 mm, length 250 mm). The EPR spectrum was acquired and used as a reference (0 min, in dark). Afterwards the sample was directly irradiated using a 365 nm LED module equipped with an optic fiber, to perform in-situ measurements. EPR spectra were acquired immediately when turning light ON and after 30 minutes. The acquired spectra were compared with spectra obtained under the same conditions, but using clean uncoated glass capillaries (control experiments).<sup>[69]</sup>

#### Photocatalytic DMPO-O<sub>2</sub>•— detection experiment

A solution of 5,5-Dimethyl-1-pyrroline N-oxide (DMPO) (5  $\mu$ g, 0.04 mmol) in CH<sub>3</sub>CN (3 mL) was prepared in a 4 mL glass vial. The solution was flushed via the double needle technique with O<sub>2</sub> for 2 minutes. The most active catalyst (50M-50P) was prepared under the same reaction conditions, and it was introduced into a capillary (IntraMark, volume 50  $\mu$ L, purchased from BRAND GMBH + CO KG) that was sealed in the flame of a gas burner from one side. The capillary was charged with an aliquot of DMPO solution in CH<sub>3</sub>CN (20  $\mu$ L, 0.01 mol $\cdot$ L<sup>-1</sup>). The open end of the capillary was sealed in the flame of gas burner and placed into an EPR tube (ID 3 mm, OD 4 mm, length 250 mm). The EPR spectrum was acquired and used as a reference (0 min, in dark). Afterwards the sample was directly irradiated using a 365 nm LED module equipped with an optic fiber, to perform in-situ measurements. EPR spectra were acquired immediately after turning the light source ON and after 30 minutes. The acquired spectra were compared with the spectra obtained under the same conditions, but using clean uncoated glass capillaries (control experiments).<sup>[69]</sup>

Irradiance of the LED modules was measured using PM400 Optical Power and Energy Meter equipped with the integrating sphere S142C and purchased from Thorlabs.

Emission spectra of LED modules were measured using Avantes spectrometer Avaspec-ULS2048CL-EVO-R5 coupled with Thorlabs optical fiber M113L01 -  $\varnothing$ 400  $\mu$ m.

### 4.5. Performance Tests

#### 4.5.1. Photooxidation of benzylamine

In a vial of 4 mL, 5 mg of catalyst are weighted, 5  $\mu$ L of benzylamine and 1 mL of acetonitrile are added. The vial is saturated with O<sub>2</sub> atmosphere for 2 min. The vial is stirred at 800 rpm and exposed to a monochromatic LED green lamp light (535nm, 50W) for 48 h. After the reaction, a few  $\mu$ L are taken to fill the third part of a gas chromatography (GC) vial and completed with acetonitrile to quantify the resulting conversion to dibenzylimine via GC. The unconverted benzylamine is also quantified for internal control, both against a calibration curve using a standard dibenzylimine solution in **Fig. S15**.

#### 4.5.2. Electrochemical Oxygen Evolution

The electrochemical measurements, cyclic/linear sweep voltammetry (CV/LSV) and chronoamperometry (CA), were performed using the same 3 electrode cell as for the Mott-Schottky experiments. LSV and CV curves were acquired at 10 and 30 mV/s of scan rate, respectively. The electrode potentials in all curves were converted to the reversible hydrogen electrode (RHE) scale using the following equation:  $E(\text{RHE}) = E(\text{Ag}/\text{AgCl}) + 0.197 + 0.059 \times \text{pH}$  V. The onset of the oxygen evolution reaction (OER) was chosen as a potential needed to reach a current density of 0.25 mA/cm<sup>2</sup>.

#### 4.5.3. Electrochemical Impedance Spectroscopy

Nyquist plots were obtained by measuring the galvanic electrochemical impedance spectroscopy (EIS). EC-Lab software was used to extract from the Nyquist plot the two resistances (electronic and charge transfer) and capacitance values by using the circuit R1/(R2+C2) configuration.

#### 4.5.4. Photoelectrochemical Test

For photoelectrochemical measurements the same electrochemical (3 electrodes) cell was used but with a white LED lamp (550.3 mW cm<sup>-2</sup> at 8 cm distance, 50W) at 4 cm distance from the working electrode to assess the photo response of the as-prepared materials. The emission spectra is in **Fig. S9**.

### **Acknowledgements**

P.J-C acknowledges Prof. Antonietti for his management support and fruitful scientific discussions. Baris Kumru and Stefano Mazzanti are thanked for fruitful discussions. The authors thank Daniel Werner for XRD, Antje Voelkel for TGA-MS and elemental analysis, and Marco Bott for electrochemistry cell assistance. The authors thank the Max Planck Society for its financial support.

The X-ray photoelectron (XPS) data collection was performed at the EPSRC National Facility for XPS (“HarwellXPS”), operated by Cardiff University and UCL, under Contract No. PR16195.

Open access funding enabled and organized by Projekt DEAL.

### **Conflict of Interest**

The authors declare no conflict of interest.

### **References**

- [1] G. Allard Reigstad, P. Coussy, J. Strasu, C. Bordin, S. Jaenhert, S. Størset, B. Ruff, *Hydrogen for Europe - Final report of the pre-study*, **2019**.
- [2] A. Galushchinskiy, R. González-Gómez, K. McCarthy, P. Farràs, A. Savateev, *Energy and Fuels* **2022**, *36*, 4625.
- [3] P. Jiménez-Calvo, V. Caps, V. Keller, *Renew. Sustain. Energy Rev.* **2021**, *149*, 111095.
- [4] National Renewable Energy Laboratory (NREL), *Reference Air Mass 1.5 Spectra | Grid Modernization | NREL*.

- [5] L. Palmisano, S. Yurdakal, Eds., *Photoelectrocatalysis : fundamentals and applications.*, First Edit., Elsevier, **2022**.
- [6] Y. Wang, A. Vogel, M. Sachs, R. Sebastian Sprick, L. Wilbraham, S. J. A. Moniz, R. Godin, M. A. Zwijnenburg, J. R. Durrant, A. I. Cooper, J. Tang, *Nat. Energy* **2019**, *4*, 746.
- [7] T. O. of E. Complexity, *Imines, derivatives, salts thereof*.
- [8] R. W. Layer, *Chem. Rev.* **1963**, *63*, 489.
- [9] V. A. Saveleva, L. Wang, D. Teschner, T. Jones, A. S. Gago, K. A. Friedrich, S. Zafeiratos, R. Schlögl, E. R. Savinova, *J. Phys. Chem. Lett.* **2018**, *9*, 3154.
- [10] T. Reier, D. Teschner, T. Lunkenbein, A. Bergmann, S. Selve, R. Kraehnert, R. Schlögl, P. Strasser, *J. Electrochem. Soc.* **2014**, *161*, F876.
- [11] S. Laha, Y. Lee, F. Podjaski, D. Weber, V. Duppel, L. M. Schoop, F. Pielnhofer, C. Scheurer, K. Müller, U. Starke, K. Reuter, B. V. Lotsch, *Adv. Energy Mater.* **2019**, *9*, 1803795.
- [12] M. Barroso, C. A. Mesa, S. R. Pendlebury, A. J. Cowan, T. Hisatomi, K. Sivula, M. Grätzel, D. R. Klug, J. R. Durrant, *Proc. Natl. Acad. Sci. U. S. A.* **2012**, *109*, 15640.
- [13] C. A. Mesa, L. Francàs, K. R. Yang, P. Garrido-Barros, E. Pastor, Y. Ma, A. Kafizas, T. E. Rosser, M. T. Mayer, E. Reisner, M. Grätzel, V. S. Batista, J. R. Durrant, *Nat. Chem.* **2019**, *12*, 82.
- [14] C. Jiang, S. J. A. Moniz, A. Wang, T. Zhang, J. Tang, *Chem. Soc. Rev* **2017**, *46*, 4645.
- [15] M. Grätzel, *Nature* **2001**, *414*, 338.
- [16] N. Karjule, C. Singh, J. Barrio, J. Tzadikov, I. Liberman, M. Volokh, E. Palomares, I. Hod, M. Shalom, N. Karjule, C. Singh, J. Barrio, J. Tzadikov, I. Liberman, M. Volokh, I. Hod, M. Shalom, E. Palomares, *Adv. Funct. Mater.* **2021**, *31*, 2101724.
- [17] A. K. Geim, K. S. Novoselov, *Nat. Mater.* **2007**, *6*, 183.
- [18] F. Haase, B. V Lotsch, *Chem. Soc. Rev* **2020**, *49*, 8469.
- [19] Q. Xu, W. Li, L. Ding, W. Yang, H. Xiao, W. J. Ong, *Nanoscale* **2019**, *11*, 1475.
- [20] J. Li, X. Gao, B. Liu, Q. Feng, X. B. Li, M. Y. Huang, Z. Liu, J. Zhang, C. H. Tung, L. Z. Wu, *J. Am. Chem. Soc.* **2016**, *138*, 3954.
- [21] X. Wang, K. Maeda, A. Thomas, K. Takanabe, G. Xin, J. M. Carlsson, K. Domen, M. Antonietti, *Nat. Mater.* **2009**, *8*, 76.
- [22] M. J. Bojdys, J.-O. Müller, M. Antonietti, A. Thomas, *Chemistry* **2008**, *14*, 8177.
- [23] J. Zhang, J. Sun, K. Maeda, K. Domen, P. Liu, M. Antonietti, X. Fu, X. Wang, *Energy Environ. Sci.* **2011**, *4*, 675.
- [24] J. P. Paraknowitsch, A. Thomas, *Energy Environ. Sci.* **2013**, *6*, 2839.
- [25] J. Barrio, M. Volokh, M. Shalom, *J. Mater. Chem. A* **2020**, *8*, 11075.
- [26] S. Hennessey, P. Farràs, *ChemPhotoChem* **2018**, *2*, 136.
- [27] D. Dontsova, S. Pronkin, M. Wehle, Z. Chen, C. Fettkenhauer, G. Clavel, M. Antonietti, *Chem. Mater.* **2015**, *27*, 5170.
- [28] D. Dontsova, C. Fettkenhauer, V. Papaefthimiou, J. Schmidt, M. Antonietti, *Chem. Mater.* **2016**, *28*, 772.
- [29] A. Savateev, S. Pronkin, J. D. Epping, M. G. Willinger, M. Antonietti, D. Dontsova, *J. Mater.*

- Chem. A* **2017**, *5*, 8394.
- [30] D. Schwarz, Y. S. Kochergin, A. Acharjya, A. Ichangi, M. V. Opanasenko, J. Čejka, U. Lappan, P. Arki, J. He, J. Schmidt, P. Nachtigall, A. Thomas, J. Tarábek, M. J. Bojdys, *Chem. – A Eur. J.* **2017**, *23*, 13023.
- [31] H. Wang, Y. Bian, J. Hu, L. Dai, *Appl. Catal. B Environ.* **2018**, *238*, 592.
- [32] S. Stolbov, S. Zuluaga, *J. Phys. Condens. Matter* **2013**, *25*, 085507.
- [33] B. Zhu, B. Cheng, L. Zhang, J. Yu, *Carbon Energy* **2019**, *1*, 32.
- [34] J. Hong, X. Xia, Y. Wang, R. Xu, *J. Mater. Chem.* **2012**, *22*, 15006.
- [35] L. L. Feng, Y. Zou, C. Li, S. Gao, L. J. Zhou, Q. Sun, M. Fan, H. Wang, D. Wang, G. D. Li, X. Zou, *Int. J. Hydrogen Energy* **2014**, *39*, 15373.
- [36] A. Savateev, S. Pronkin, J. D. Epping, M. G. Willinger, C. Wolff, D. Neher, M. Antonietti, D. Dontsova, *ChemCatChem* **2017**, *9*, 167.
- [37] A. Cousson, B. Nicolai, F. Fillaux, *Acta Crystallogr. Sect. E Struct. Reports Online* **2005**, *61*, o222.
- [38] B. V. Lotsch, M. Döblinger, J. Sehnert, L. Seyfarth, J. Senker, O. Oeckler, W. Schnick, *Chem. – A Eur. J.* **2007**, *13*, 4969.
- [39] B. Jürgens, E. Irran, J. Senker, P. Kroll, H. Müller, W. Schnick, *J. Am. Chem. Soc.* **2003**, *125*, 10288.
- [40] V. W. hei Lau, B. V. Lotsch, *Adv. Energy Mater.* **2021**, 2101078.
- [41] B. V. L. and, W. Schnick\*, *Chem. Mater.* **2006**, *18*, 1891.
- [42] I. Papailias, T. Giannakopoulou, N. Todorova, D. Demotikali, T. Vaimakis, C. Trapalis, *Appl. Surf. Sci.* **2015**, *358*, 278.
- [43] P. Jiménez-Calvo, C. Marchal, T. Cottineau, V. Caps, V. Keller, *J. Mater. Chem. A* **2019**, *7*, 14849.
- [44] A. Thomas, A. Fischer, F. Goettmann, M. Antonietti, J.-O. Müller, R. Schlögl, J. M. Carlsson, *J. Mater. Chem.* **2008**, *18*, 4893.
- [45] Y. Wang, X. Wang, M. Antonietti, *Angew. Chem. Int. Ed. Engl.* **2012**, *51*, 68.
- [46] X. Wang, S. Blechert, M. Antonietti, *ACS Catal.* **2012**, *2*, 1596.
- [47] R. C. Haddon, S. R. Wasserman, F. Wudl, G. R. J. Williams, *J. Am. Chem. Soc.* **1980**, *102*, 6687.
- [48] Y. Kang, Y. Yang, L.-C. Yin, X. Kang, G. Liu, H.-M. Y. Cheng Kang, Y. Yang, L. Yin, X. Kang, G. Liu, H. Cheng, *Adv. Mater.* **2015**, *27*, 4572.
- [49] Y. Chen, B. Wang, S. Lin, Y. Zhang, X. Wang, *J. Phys. Chem. C* **2014**, *118*, 29981.
- [50] A. B. Jorge, D. J. Martin, M. T. S. Dhanoa, A. S. Rahman, N. Makwana, J. Tang, A. Sella, F. Corà, S. Firth, J. A. Darr, P. F. McMillan, *J. Phys. Chem. C* **2013**, *117*, 7178.
- [51] A. Savateev, N. V. Tarakina, V. Strauss, T. Hussain, K. ten Brummelhuis, J. M. Sánchez Vadillo, Y. Markushyna, S. Mazzanti, A. P. Tyutyunnik, R. Walczak, M. Oschatz, D. M. Guldi, A. Karton, M. Antonietti, *Angew. Chemie - Int. Ed.* **2020**, *59*, 15061.
- [52] Y. Markushyna, C. M. Schüßlbauer, T. Ullrich, D. M. Guldi, M. Antonietti, A. Savateev, *Angew. Chemie Int. Ed.* **2021**, *60*, 20543.

- [53] M. Shalom, S. Inal, C. Fettkenhauer, D. Neher, M. Antonietti, *J. Am. Chem. Soc.* **2013**, *135*, 7118.
- [54] A. Hankin, F. E. Bedoya-Lora, J. C. Alexander, A. Regoutz, G. H. Kelsall, *J. Mater. Chem. A* **2019**, *7*, 26162.
- [55] P. Jiménez-Calvo, V. Caps, M. N. Ghazzal, C. Colbeau-Justin, V. Keller, *Nano Energy* **2020**, *75*, 104888.
- [56] A. Thirumoorthi, K. P. Elango, *J. Chem. Sci* **2007**, *119*, 289.
- [57] A. Thirumoorthi, K. P. Elango, *Int. J. Chem. Kinet.* **2007**, *39*, 371.
- [58] M. A. R. da Silva, I. F. Silva, Q. Xue, B. T. W. Lo, N. V. Tarakina, B. N. Nunes, P. Adler, S. K. Sahoo, D. W. Bahnemann, N. López-Salas, A. Savateev, C. Ribeiro, T. D. Kühne, M. Antonietti, I. F. Teixeira, *Appl. Catal. B Environ.* **2022**, *304*, 120965.
- [59] K. Takanabe, *ACS Catal.* **2017**, *7*, 8006.
- [60] S. Brunauer, P. H. Emmett, E. Teller, *J. Am. Chem. Soc.* **1938**, *60*, 309.
- [61] X. Wang, K. Maeda, A. Thomas, K. Takanabe, G. Xin, J. M. Carlsson, K. Domen, M. Antonietti, *Nat. Mater.* **2009**, *8*, 76.
- [62] H. El Marouazi, P. Jiménez-Calvo, E. Breniaux, C. Colbeau-Justin, I. Janowska, V. Keller, *ACS Sustain. Chem. Eng.* **2021**, *9*, 3633.
- [63] Z. Tong, D. Yang, T. Xiao, Y. Tian, Z. Jiang, *Chem. Eng. J.* **2015**, *260*, 117.
- [64] N. D. Shcherban, S. M. Filonenko, M. L. Ovcharov, A. M. Mishura, M. A. Skoryk, A. Aho, D. Y. Murzin, *ChemistrySelect* **2016**, *1*, 4987.
- [65] B. Saner, F. Okyay, Y. Yürüm, *Fuel* **2010**, *89*, 1903.
- [66] P. I. Jiménez-Calvo, Synthesis, characterization, and performance of g-C<sub>3</sub>N<sub>4</sub> based materials decorated with Au nanoparticles for (photo) catalytic applications, Université de Strasbourg, **2019**.
- [67] W.-J. Ong, L.-L. Tan, Y. H. Ng, S.-T. Yong, S.-P. Chai, *Chem. Rev.* **2016**, *116*, 7159.
- [68] J. T. DuBose, P. V. Kamat, *Chem. Rev.* **2022**.
- [69] Y. Markushyna, P. Lamagni, J. Catalano, N. Lock, G. Zhang, M. Antonietti, A. Savateev, *ACS Catal.* **2020**, *10*, 7336.
- [70] B. L. Wadsworth, N. P. Nguyen, D. Nishiori, A. M. Beiler, G. F. Moore, *ACS Appl. Energy Mater.* **2020**.
- [71] J. Kossmann, M. María, L. Ortízortíz, S. ´ Anchez-Manjavacas, H. Zschiesche, N. V Tarakina, M. Antonietti, J. Albero, N. L ´ Opez-Salas, **2022**.
- [72] V. S. Kale, U. Sim, J. Yang, K. Jin, S. In Chae, W. Je Chang, A. Kumar Sinha, H. Ha, C.-C. Hwang, J. An, H.-K. Hong, Z. Lee, K. Tae Nam, T. Hyeon, V. S. Kale, J. Yang, S. I. Chae, A. K. Sinha, T. Hyeon, U. Sim, K. Jin, W. J. Chang, H. Ha, J. An, K. T. Nam, C. Hwang, H. Hong, Z. Lee, *Small* **2017**, *13*, 1603893.
- [73] T. J. Bandoz, J. Matos, M. Seredych, M. S. Z. Islam, R. Alfano, *Appl. Catal. A Gen.* **2012**, *445–446*, 159.
- [74] S. Wang, L. Zhang, Z. Xia, A. Roy, D. W. Chang, J. B. Baek, L. Dai, *Angew. Chem. Int. Ed. Engl.* **2012**, *51*, 4209.
- [75] K. Wang, Q. Li, B. Liu, B. Cheng, W. Ho, J. Yu, *Appl. Catal. B Environ.* **2015**, *176–177*, 44.

- [76] G. Liu, P. Niu, C. Sun, S. C. Smith, Z. Chen, G. Q. Lu, H. M. Cheng, *J. Am. Chem. Soc.* **2010**, *132*, 11642.
- [77] B. Coulson, L. Lari, M. Isaacs, D. J. Raines, R. E. Douthwaite, A. K. Duhme-Klair, *Chem. – A Eur. J.* **2020**, *26*, 6862.
- [78] B. Coulson, M. Isaacs, L. Lari, R. E. Douthwaite, A. K. Duhme-Klair, *Chem. Commun.* **2019**, *55*, 7450.
- [79] S. Qiao, R. W. Mitchell, B. Coulson, D. V. Jowett, B. R. G. Johnson, R. Brydson, M. Isaacs, A. F. Lee, R. E. Douthwaite, *Carbon N. Y.* **2016**, *106*, 320.
- [80] S. A. Shevlin, Z. X. Guo, *Chem. Mater.* **2016**, *28*, 7250.
- [81] B. Zhu, J. Zhang, C. Jiang, B. Cheng, J. Yu, *Appl. Catal. B Environ.* **2017**, *207*, 27.
- [82] A. Sillen, Y. Engelborghs, *Photochem. Photobiol.* **1998**, *67*, 475.